Hybrid 2D plasma simulations of a 20kW-class magnetically shielded Hall effect thruster

IEPC-2022-322

Presented at the 37th International Electric Propulsion Conference
Massachusetts Institute of Technology, Cambridge, MA, USA
June 19-23, 2022

Jesús Perales-Díaz [1], Adrian Domínguez-Vázquez [2], Pablo Fajardo [3] and Eduardo Ahedo [4]
Equipo de Propulsión Espacial y Plasmas (EP2), Universidad Carlos III de Madrid, 28911 Leganés, Spain

T. Andreussi [5] and A. Piragino [6]
SITAEL S.p.A., Via A. Gherardesca 5, 56121 Pisa, Italy

Numerical simulations of the HT20k, a high power magnetically-shielded Hall effect thruster, developed by SITAEL, are carried out with HYPHEN, a two-dimensional axisymmetric hybrid PIC/fluid code with a magnetized and diffusive electron transport model. The model includes a phenomenological anomalous transport parameter, which is adjusted with experimental data. A 2D spatial characterization of the plasma discharge, including profiles along the thruster walls and global balances of current and power, is presented, showing the effectiveness of the magnetic shielding topology. The simulation results show little sensitivity to the plasma-wall interaction parameters. The removal of neutral injection through the cathode leads to a weaker coupling voltage and reduces slightly the performance. When CEX collisions are included in the simulations the performance is not noticeably affected. The sensitivity of the simulation results to the downstream global boundary condition for electric current and heat fluxes is analyzed.

I. Introduction

The recent advances in Hall effect thruster (HET) systems in terms of performance and reliability, combined with an increase in the availability of onboard electric power, are leading the way for an important implementation of high power Hall effect thrusters in a wide variety of space platforms. ASPIRE (Advanced Space Propulsion for Innovative Realization of space Exploration) is an EU-funded H2020 project with the goal of increasing the Technology Readiness Level (TRL) of the HT20k thruster to 6. The HT20k thruster is a 20kW-class (high power) HET developed by SITAEL[1], which features a magnetically shielded topology with singular magnetic point, from the DM2 version onwards, to increase the thruster operational life and performance[2].

Another goal of ASPIRE is the enhancement of the numerical capabilities required to qualify high-power systems (with large cost and limited availability of test facilities), which are not sufficiently matured in Europe currently. EP2 group at UC3M, together with other two university groups, is working on the modeling of the HT20k thruster within the framework of ASPIRE, making use, for validation purposes, of the HT20k firing test data gathered by SITAEL. In

[1]PhD candidate, Bioengineering and Aerospace Engineering Department, jperales@ing.uc3m.es.
[2]Assistant professor, Bioengineering and Aerospace Engineering Department, addoming@ing.uc3m.es.
[3]Full professor, Bioengineering and Aerospace Engineering Department, pablo.fajardo@uc3m.es.
[4]Full professor, Bioengineering and Aerospace Engineering Department, eduardo.ahedo@uc3m.es.
[5]Director of SITAEL's EP technology development team, tommaso.andreussi@sitael.com
[6]Senior propulsion engineer, antonio.piragino@sitael.com

particular, EP2 numerical tool HYPHEN (HYbrid Plasma thruster Holistic simulation ENvironment)[3, 4], an advanced two-dimensional axisymmetric hybrid simulation code, is used for the simulation

HYPHEN uses a particle-in-cell(PIC) formulation for heavy species and a fluid one for electrons. The HET version of HYPHEN, developed by the EP2 group at UC3M in the frame of the CHEOPS H2020 project, was successfully adapted to the simulation of magnetically-shielded HETs, such as the HT20k, in the context of the EDDA project[5].

This paper describes a part of the numerical simulation activities and results obtained on the HT20k thruster discharge within the context of the ASPIRE project. A spatial 2D description of relevant plasma properties for a certain operational point is presented and commented, showing the effect of the magnetic topology on the plasma behavior inside the chamber. The phenomenological parameter, α_t, which accounts for the level of turbulent anomalous transport, is adjusted using experimental data of the discharge current, I_d, and the thrust, F. The sensitivity of the simulation results to several plasma-wall interaction parameters, to the cathode neutral injection and CEX collisions is tested. Moreover, the effect on the discharge of a global current boundary condition[6] is studied.

The paper is structured as follows. Section II briefly describes the thruster unit, its development and testing. Section III presents a brief description of the simulation model. Then, the simulation set-up is described in Section IV. Section V contains the simulation results and their comparison to the experimental data. Finally, the conclusions are drawn in Section VI.

II. Thruster description

The development of the HT20k started in 2015 with the first development model, the HT20k DM1 [7]. This model, with a conventional SPT like magnetic topology, was tested in 2017 for 250 hours, comprising a performance characterization and a 150-hour wear test. In 2018, the HT20k DM1 design was reviewed by implementing a magnetic shielding topology to reduce the erosion of the channel and increase the thruster lifetime. This new version was thus labelled HT20k DM2. The magnetic configuration of the HT20k DM2 was derived from the investigations performed on two different development models of SITAEL's 5 kW-class Hall thruster, the HT5k [8, 9]. Specifically, the BN-SiO2 ceramic channel was manufactured with a chamfer near its exit and the magnetic circuit was designed to have a magnetic field line almost tangent to the chamfer [10]. This line penetrates towards the colder anode region, leading to a reduced near-wall electron temperature and an electric potential closer to the anode potential. The HT20k DM2 design comprised three different configurations of the ceramic channel. These configurations, the HT20k S (small), HT20k M (medium), and HT20k L (large), feature the same channel mean diameter and differ in terms of channel width [2, 11]. The magnetic screens and poles allow for the accommodation of the different channels and the implementation of the same magnetic shielding topology.

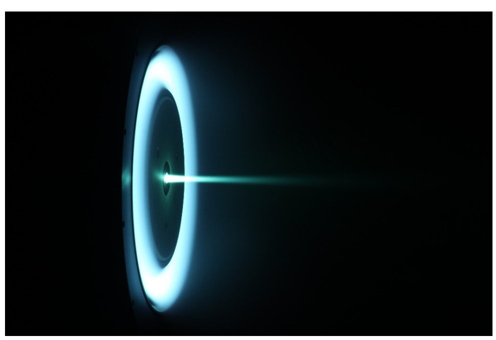

Fig. 1 HT20k DM2 (M configuration) operating at 25 mg/s and 300 V.

The present work focuses on the HT20k DM2 - M shown in Figure 1, which have the same channel dimensions of the first unshielded development model, the HT20k DM1. The HT20k DM2 Hall thruster is coupled with SITAEL's HC60 high-current hollow cathode [12], mounted in central position on the thruster axis. The cathode is designed to provide a high electron current (with a nominal operating condition of 60 A), which is necessary to maintain the discharge and to neutralize the beam. The HT20k DM2, coupled with the HC60, has been tested in two dedicated experimental campaigns, operating at up to 22.5 kW of discharge power. These tests allowed to derive experimental scaling laws for the design of high-power magnetically shielded thrusters [13], serving as a solid base for the design of the HT20k-TU engineering model (EM). The HT20k-TU EM was tested at the beginning of 2021 in the framework of the

EU H2020 CHEOPS program, showing reliable operation with krypton propellant and in a direct-drive configuration [10]. In addition, the TU EM also underwent a first full vibration test at the end of 2021. To date, the HT20k thruster family, comprehensive of the DM1, DM2 and the HT20k-TU EM fired for a total of 1800 hours [14]. Currently, the HT20k-TU design is being consolidated in the frame of the ASPIRE project, paving the way for the qualification of the first European very-high power Hall propulsion system.

III. HYPHEN model

In Fig. 2(a), the HYPHEN code structure and the simulation loop are depicted. HYPHEN is a two-dimensional (axisymmetric) hybrid particle-in-cell (PIC)/fluid, multi-thruster, OpenMP parallelized simulation code built in a modular way. The version of HYPHEN for HET's, which is the one used for the simulations shown in the following sections, is formed by three main modules: the ion module (I-module), for the simulation of the dynamics of the heavy species (i.e. ions and neutrals), following a Lagrangian approach; the electron module (E-module), which solves a fluid model for the magnetized electron population and applies quasineutrality; and a sheath module (S-module) to match the conditions at the thruster walls with the quasineutral plasma by solving the Debye sheaths, which are discontinuity surfaces in the model. The coupling of the modules is visible in Fig. 2(a) for a time-step of the simulation. The simulation loop is described in [5].

The I-module, whose detailed explanation can be found in Refs. [3, 15, 16], operates on a structured mesh of the simulation domain, shown in Fig. 2(b), to obtain the particle densities and fluxes for the different neutral and ion populations. On the other hand, and in order to limit the numerical diffusion arising from the strong anisotropic transport on magnetized electrons, the E-module uses an unstructured magnetic field aligned mesh (MFAM) [17], defined by the externally applied magnetic field $\boldsymbol{B}$ and shown in Fig. 2(c). The E-module solves a quasineutral, drift-diffusion fluid model for the magnetized electron population, obtaining the electric potential, ϕ, electron temperature, T_e, and the electron current density and heat flux vectors $\boldsymbol{j}_e$ and $\boldsymbol{q}_e$, respectively. The detailed explanation of the fluid model for the electrons can be found in Refs. [5, 18]. The interpolation module enables the communication between both the I and E-modules. In Figs. 2(b) and (c), L_c and H_c are the chamber length and the chamber width, respectively.

HYPHEN includes a turbulent or anomalous force, $\boldsymbol{F}_t$, in the electron momentum equation. These turbulent force, accounting for time and azimuth-averaged, high-frequency, wave-based anomalous transport, is modeled empirically as [19–22]

$$\boldsymbol{F}_t \simeq -m_e \nu_t n_e u_{\theta e} \mathbf{1}_\theta, \qquad \nu_t = \alpha_t \omega_{ce}, \tag{1}$$

with ν_t a turbulent collision frequency, $\omega_{ce} = eB/m_e$ the electron gyrofrequency, and $\alpha_t(z, r)$ a empirical function representing the local turbulence level [19, 22], which is tuned using experimental data. Turbulent-based contributions to the axial and radial momentum equations can be neglected with respect to the other terms of the equations.

A detailed description of the numerical treatment of the electron fluid equations in the unstructured, irregular MFAM can be found in Refs. [17, 18, 23, 24]. Here, only some relevant information about the boundary conditions will be mentioned. These are imposed at each MFAM boundary face in terms of ϕ, T_e, $j_{ne} = \mathbf{1}_n \cdot \boldsymbol{j}_e$ and $q_{ne} = \mathbf{1}_n \cdot \boldsymbol{q}_e$, with $\mathbf{1}_n$ being the *outward* unit normal vector. The reference potential, $\phi = 0$, is set in all the cathode faces. This implies that the anode potential is $\phi = V_d$. The sheath edge of the quasineutral plasma, modeled by the boundary faces of the MFAM, encloses the domain. The solution for the (infinitely) thin Debye sheaths, computed by the S-module, is described in the Appendix of Ref. [5] and omitted here.

At a dielectric wall, local zero-current condition is imposed, $j_{ne} = -j_{ni}$. At the anode, with potential equal to the discharge voltage, V_d, the determination of j_{ne} and q_{ne}, at each anode face of the MFAM, requires to iterate to solve for $\Delta\phi_{sh}$ (refer to Ref. [5] for further details). At the cathode boundary faces, j_{ne} is obtained from I_d and the cathode surface area. At the (quasineutral) axis, symmetry conditions are imposed.

At the plume downstream boundary of the simulation domain P [blue boundary line in Fig. 2(b)], a global downstream matching layer (GDML) model provides expressions for j_{ne} and q_{ne}[6]. The GDML is defined as a thin boundary layer providing the jump conditions for relevant electron magnitudes between P and the infinity, where a final electric potential far downstream ϕ_∞ is reached and a global current free condition $I_\infty = 0$ is expected. A first version of the GDML (partially similar to a classical Debye sheath) is implemented in HYPHEN, so that the final potential ϕ_∞ is obtained by imposing a global zero current condition at P, so that $I_{e,\infty} = -I_{i,\infty}$. A downstream potential ϕ_∞ can also be set by the user to obtain $I_\infty \neq 0$, as done in Sec. V.E. The schematic representation of the GDML is shown in Fig. 3.

The time discretization of the electron equations follows a semi-implicit scheme [18, 24, 25], with a sub-timestep $\Delta t_e = \Delta t / N_e$ and $N_e = O(1)$.

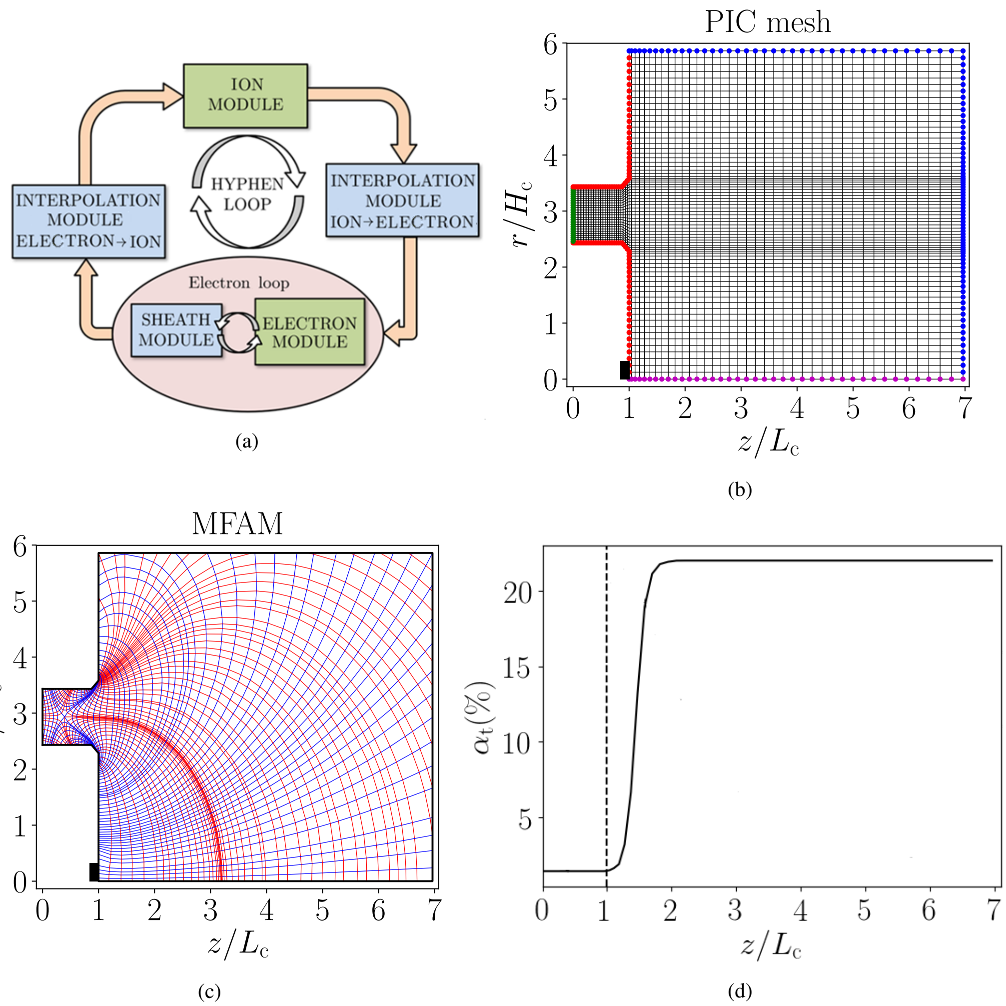

Fig. 2 (a) Simplified description of HYPHEN time-integration loop. (b) Cylindrical mesh used by the I-module. The red, green, blue and magenta lines indicate the thruster dielectric walls, the anode, the plume downstream boundary P, and the symmetry axis, respectively. The centrally-mounted cathode is indicated by the small black box. (c) The MFAM used by the E-module. Blue and red lines are B-parallel and B-perpendicular lines, respectively, defining the cells. (d) 1D axial profiles along the thruster channel midline of the "step-out" type α_t function used for all simulation cases presented in this work

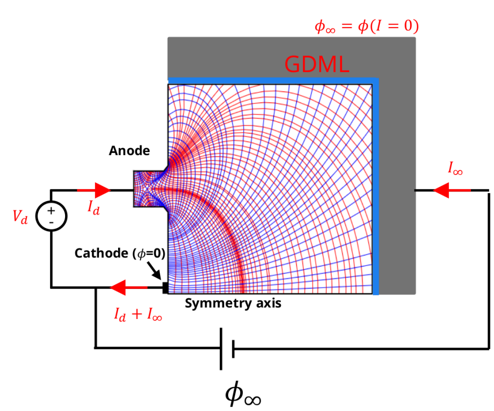

Fig. 3 Sketch representing the infinity-to-cathode bias ϕ_∞ obtained through the GDML condition.

IV. Simulation set-up

This section describes the reference simulation set-up for the HT20k simulations presented here. Figs. 2(b) and 2(c) show the PIC mesh and the MFAM used to simulate the HT20k. The main characteristics of the meshes and the relevant simulation parameters are listed in Table. 1. A singular magnetic point ($\boldsymbol{B} = 0$) is located inside the thruster chamber. The green line at the left boundary in Fig. 2(b) indicates the position of the annular anode wall, while the small black box in Fig. 2(c) represents the central cathode, which is modeled as a surface boundary.

The selected xenon mass flow $\dot{m}_{\mathrm{A}}$ is injected from a Maxwellian reservoir through a portion of the annular anode, from $r/H_{\mathrm{c}} = 2.74$ to $r/H_{\mathrm{c}} = 3.12$. The injection is performed with a flat profile, a given temperature and sonic fluid velocity (Table. 1). With the same properties, a neutral mass flow $\dot{m}_{\mathrm{C}}$ is injected through the cathode surface. The emission energy of electrons at the cathode is set to $2T_c = 4.5$eV [26].

Ions are recombined into neutrals at the material walls. Singly and doubly charged ions are produced inside the simulation volume by collisions of electrons and neutrals. The single ionization rates considered by HYPHEN come from the BIAGI database [27]. The double ionization rates are obtained from the Drawin model [28], including the reactions $A + e \rightarrow A^{++} + 3e$, and $A^{+} + e \rightarrow A^{++} + 2e$. Neutrals are reinjected diffusely after ion recombination, considering complete energy accomodation, with the energy of the walls, which is set to 850K [29]. Moreover, neutrals undergo a quasi-specular reflection at the walls according to the Schamberg model [30, 31] with complete energy accommodation; Refs. [3, 16] provide further details on the interaction of heavy-species macroparticles with walls. Each macroparticle population is controlled by the I-module, targeting a number of 100 macroparticles per cell of each population with a $\pm 10\%$ of tolerance [3].

The sheath model includes elastically reflected electrons and secondary electron emission (SEE) from the walls, and also retains other non-Maxwellian features of the electron VDF [32], such as the replenishment fraction of the high energy tails of the electron VDF through the parameter σ_{rp}. The yields for the elastically reflected electrons and the secondary ones are, respectively:

$$\delta_{\mathrm{r}}(T_{\mathrm{e}}) = \delta_{\mathrm{r0}} E_{\mathrm{r}}^2/(T_{\mathrm{e}} + E_{\mathrm{r}})^2, \tag{2}$$

$$\delta_{\mathrm{s}}(T_{\mathrm{e}}) = \min\left(2T_{\mathrm{e}}/E_1, \delta_{\mathrm{s}}^*\right), \tag{3}$$

with δ_{r0}, E_{r} and E_1 being material dependent parameters, and δ_{s}^* the effective upper-bounded SEE yield, corresponding to a space-charge limited (SCL) sheath with $e\Delta\phi/T_{\mathrm{e}} = 1$. At boron nitride dielectric walls, we take $E_1 = 50$ eV, $\delta_{\mathrm{r0}} = 0.4$ and $E_{\mathrm{r}} = 20$ eV. Additionally, the replenishment fraction of the electron VDF is $\sigma_{\mathrm{rp}} = 0.1$. The metallic anode features no SEE.

The (ion) timestep is set in such a way that an averaged doubly-charged ion takes, as minimum, two timesteps to cross the smallest cell of the PIC mesh. To start the simulations, neutrals are injected through the anode and cathode and a minimum background plasma density is considered to trigger the discharge [16]. The simulations are run for a total of 60000 timesteps (900 μs of simulation time), to observe a sufficiently large number of low-frequency (i.e. breathing mode) oscillation cycles of I_{d}. Five sub-timesteps per ion timestep ($N_{\mathrm{e}} = 5$) are considered to integrate the electron equations [3]. To obtain the contour and profile plots shown in the next sections, the plasma variables are averaged over several I_{d} cycles.

Table 1 Main simulation parameters and mesh characteristics.

Simulation parameter	Units	Value
PIC mesh number of cells, nodes	-	5328, 5475
PIC mesh smallest grid size	mm	1
MFAM number of cells, faces	-	3980, 7794
MFAM average skewness [33]	-	0.059
Ion-moving timestep, Δt	ns	15
Total number of simulation steps	-	60000
Injected Xe velocity	ms^{-1}	300
Injected Xe temperature	K	850

V. Results

A. Analysis of the 2D plasma discharge

In this section, the results of the simulation of the HT20k for one (reference) operation point are presented and analysed. This operation point is described in Table. 2.

Table 2 Reference operation point for xenon as propellant defined in terms of anodic mass flow rate, $\dot{m}_A$, cathode mass flow rate, $\dot{m}_C$, source voltage, V_s, background pressure, p_{Xe}.

$\dot{m}_A$ (mg/s)	$\dot{m}_C$ (mg/s)	V_s (V)	p_{Xe}(mbar)	Mag. Field (mT)
20	1.5	300	1.5E-5	21

The electron model requires the tuning of the turbulent parameter $\alpha_t(z, r)$ in Eq. (1) for the operation point to be simulated. To do that, the experimental values of I_d and F are targeted to tune the function α_t following a "step-out" profile with two fitting parameters only, α_{t1} and $\alpha_{t2}(> \alpha_{t1})$, applied, approximately, inside and outside the thruster chamber, respectively. Step-out profiles have performed well in previous studies [34–37]. Fig. 2(d) shows the axial step-out profile used in this work, where the transition from α_{t1} to α_{t2} takes place close to the maximum magnetic field point along the thruster channel midline. A particular step-out profile will referred to as (α_{t1}, α_{t2}).

The pair (α_{t1}, α_{t2}) = (0.014, 0.22) is tuned to reproduce the experimental values (I_d, F) with an error below 5% (the reported experimental data repeatability). Table. 3 summarizes the simulation results. The tuning process has revealed the following behaviour. The value of α_{t1} affects mainly I_d, which increases for larger values of α_{t1}, while F is barely affected. On the other hand, both I_d and F increase for larger α_{t2}. The relatively high value of α_{t2} (almost three times larger than that found for the case of the HT5k thruster [5]) is needed to match the experimentally reported F value. Nonetheless, this aspect is under further current investigation.

Table 3 Simulation results for the best fit of the turbulent profile (first column). Time-averaged values of I_d and F. The dominant frequency of I_d oscillations f_d and the relative discharge current half-amplitude, $\Delta I_d/I_d$ are also included.

(α_{t1}, α_{t2}) %	I_d (A)	F (mN)	f_d (kHz)	$\Delta I_d/I_d$ (%)
(1.4, 22.0)	22.6	385	12.1	± 5.0

The turbulence fitting reproduces well the so-called breathing mode [20, 38–40] that dominates the I_d oscillations. Figs. 4 (a) and 4 (b) show the time evolution of I_d and its normalized amplitude spectrum, respectively. The simulation yields a value of the dominant frequency of the I_d oscillations f_d = 12.1 kHz, close to the 11 kHz reported in experiments.

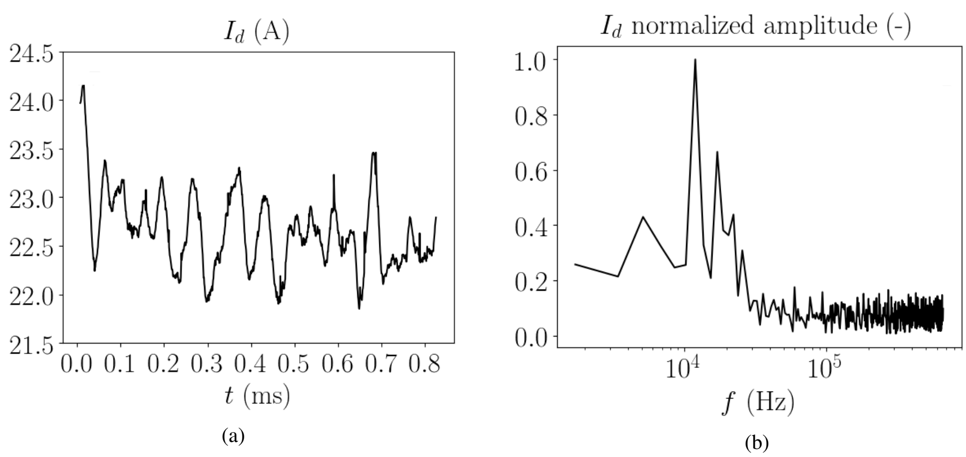

Fig. 4 (a) Time evolution of I_d, (b) I_d normalized amplitude spectrum for the reference case.

Figs. 5(black lines only) and 6 show the profile and contour plots, respectively, of relevant time-averaged plasma magnitudes of the discharge both inside the thruster chamber and in the near plume. In Fig. 6, the left column presents a zoom of the chamber of the thruster, while the right column shows the complete domain, including the chamber and the plume region. The plasma magnitudes shown are the neutral density n_n, the plasma density n_e, the electric potential ϕ, and the electron temperature T_e.

Figs. 5(a) and 6(a) show the neutral density profile and 2D contour inside the chamber. The effects of neutral gas injection from the anode wall, gas ionization and neutral emission from the lateral walls due to ion recombination are present. The neutral density decreases about 3 orders of magnitude inside the thruster chamber, corresponding to a large propellant utilization. Fig. 6(b) shows the injection of the neutrals through the cathode, which is also noticeable in the black line of Fig. 5(a), with the increase in neutral density downstream the channel exit, where the cathode neutral plume merges with the one exiting the thruster chamber. The high neutral density around the cathode results in a significant ionization there, as seen in Fig. 6(d). Moreover, the enhanced electron-neutral collisionality favors the coupling of cathode electrons with the main ion beam. Fig. 6(c) reveals higher plasma density values and a more uniform plasma density distribution inside the chamber than in conventional HETs. As usual, the plasma density features a peak at a central region of the chamber, close to the magnetic singular point in this case. In the near plume, plasma density decreases due to ion acceleration and expansion. Fig. 6(d) shows the secondary plasma plume created by ionization of cathode neutrals, which merges downstream with the main one. As shown in Fig. 6(e), the electric potential peak inside the chamber is located at a central region slightly downstream the n_e peak. As expected in a HET MS configuration, the electric potential is rather flat inside the chamber, which greatly reduces wall erosion. The MS moves most of the ion acceleration region outside the chamber, where equipotential lines follow approximately magnetic field lines. Inside the thruster chamber, the magnetic null point and pressure gradients uncouple magnetic and equipotential lines. The black line in Fig. 5(c) shows that ϕ falls down to 50 V in an axial distance of 2 chamber lengths from the thruster chamber exit plane, approximately. The electron temperature peak is around 50 eV, and located in the near plume, close to the point with maximum axial electric field. Temperature isolines closely follow magnetic lines, and steep gradients are found upstream the T_e peak, where the electron flow enters into the thruster chamber. Downstream, T_e falls down to around 10 eV in a distance of the order of 1-2 chamber lengths from the thruster channel exit. The effectiveness of the HT20k MS topology is revealed in Fig. 6(g), where the thruster chamber walls are surrounded by temperature isolines with T_e below 5 eV. This is one of the main achievements of MS topologies and leads to small energy losses to the walls and low ion wall-impact energy.

Fig. 7 shows the longitudinal (i.e. in-plane) ion $\tilde{\boldsymbol{j}}_\mathrm{i}$, electron $\tilde{\boldsymbol{j}}_\mathrm{e}$ and electric $\tilde{\boldsymbol{j}}$ current densities, which are defined as $\tilde{\boldsymbol{j}}_i = \boldsymbol{j}_i - j_{\theta\mathrm{i}}\mathbf{1}_\theta$ and so on. Most of the ionization of the neutral gas is distributed in the whole chamber volume. The ion streamlines represent the macroscopic behaviour of the ion population, and reveal the existence of significant ion currents collected at the anode and lateral chamber walls, and a central region with $\tilde{j}_\mathrm{i} \sim 0$ close to the magnetic null point. Ions, which are practically unmagnetized, follow the electric field, and are not prevented from impacting the channel walls. Fig. 7(a) shows nearly wall-parallel ion streamlines close to the channel exit. In the near plume region, ion streamlines reveal the expected ion divergence characterizing the beam expansion. The cathode-born electron streamlines shown in Fig. 7(d) split into two electron beams: one flows downstream to neutralize the main ion beam, and the other progressively moves across the magnetic field into the thruster chamber to ionize the injected neutral gas and sustain the discharge. This second beam is channeled by the magnetic lines close to the magnetic null point inside the thruster chamber, but still some electron streamlines are collected to the lateral walls to cancel the ion flow and thus satisfy the dielectric condition imposed there. The simulation results reveal that the splitting of the cathode electron streamlines takes place over almost the whole axial extent of the near plume region simulated. The electron streamlines exhibit rather abrupt turns close to the plume downstream boundary. This situation differs from that reported in Ref. [5] for the HT5k, where the enhanced electron cross-field transport due to the neutral injection through the cathode provided a much smoother coupling of the cathode electrons with the ion beam. Here, the results suggest that the simulation domain should be extended downstream to better capture the cathode-beam coupling. This aspect requires further investigation. Finally, Figs. 7(e) and 7(f) show the 2D streamlines of the longitudinal electric current. At the chamber lateral walls, the net electric current collected is locally null, and the ion flows in Fig. 7(a) are canceled by the electron ones in Fig. 7(c). While the expected current loops connecting anode and cathode are found, in the near plume a second current loop closing at infinity develops from the GDML condition imposed at the downstream plume boundary, which decouples local ion and electron currents. Through the lateral plume boundary, electric current flows into the domain, as a result of the electron flow dominating over the ion stream there. This current leaves the domain through the vertical (i.e., axial) downstream boundary, mainly near the symmetry axis, where the ion current dominates, thus assuring zero total current collected at the downstream plume boundary.

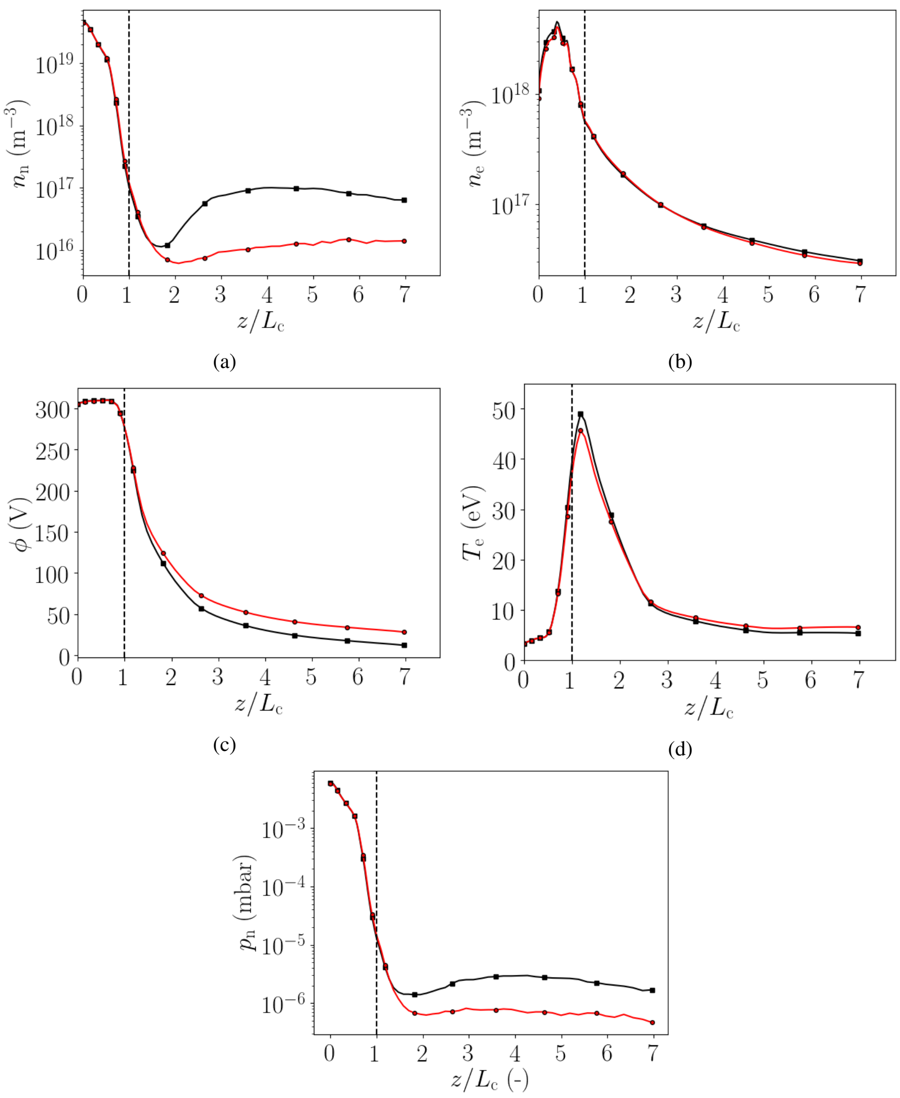

(a) (b) (c) (d) (e)

Fig. 5 Time-averaged 1D axial profiles along the thruster chamber midline for cases with cathode injection (black line with square markers) and without cathode injection (red line with circle markers). Magnitude of (a) neutral density n_n, (b) plasma density n_e, (c) electric potential ϕ, (d) electron temperature T_e and (e) neutral pressure, p_n.

In order to study more in detail the MS effects, Fig. 8 shows relevant plasma magnitudes plotted along the thruster chamber internal walls. The abscissa length coordinate s runs along the whole chamber wall, from the end of the inner chamfer to the end of the outer chamfer. Thus, it goes first along the inner lateral wall, then along the anode, and finally, along the outer lateral wall. The analysis in this section refers only to the black line, which corresponds to the reference case. Fig. 8(a) shows a flat ϕ profile along the sheath edge around the chamber walls, with ϕ close to V_s = 300 V, and confirms that the MS configuration moves most of the acceleration region outside the thruster chamber. Only at the end of both chamfers ϕ drops below 300 V, reaching ~275 V at the chamber exit inner corner. Figs. 8(b) and 8(c) show the sheath potential fall and the electron temperature at the sheath edge. The electron temperature is low (~2-5 eV) and the ratio $e\Delta\phi/T_\mathrm{e}$ is between 1 and 3. At the anode wall, this ratio controls the local electron flux. At dielectric walls, this ratio is affected by the SEE yield δ_s and the replenishment of the electron VDF, modeled through σ_rp. The low T_e yields small δ_s values, ranging between 0.1 and 0.2.

Fig. 8(d) plots the electron and ion currents towards the walls (whose values do not change across the Debye

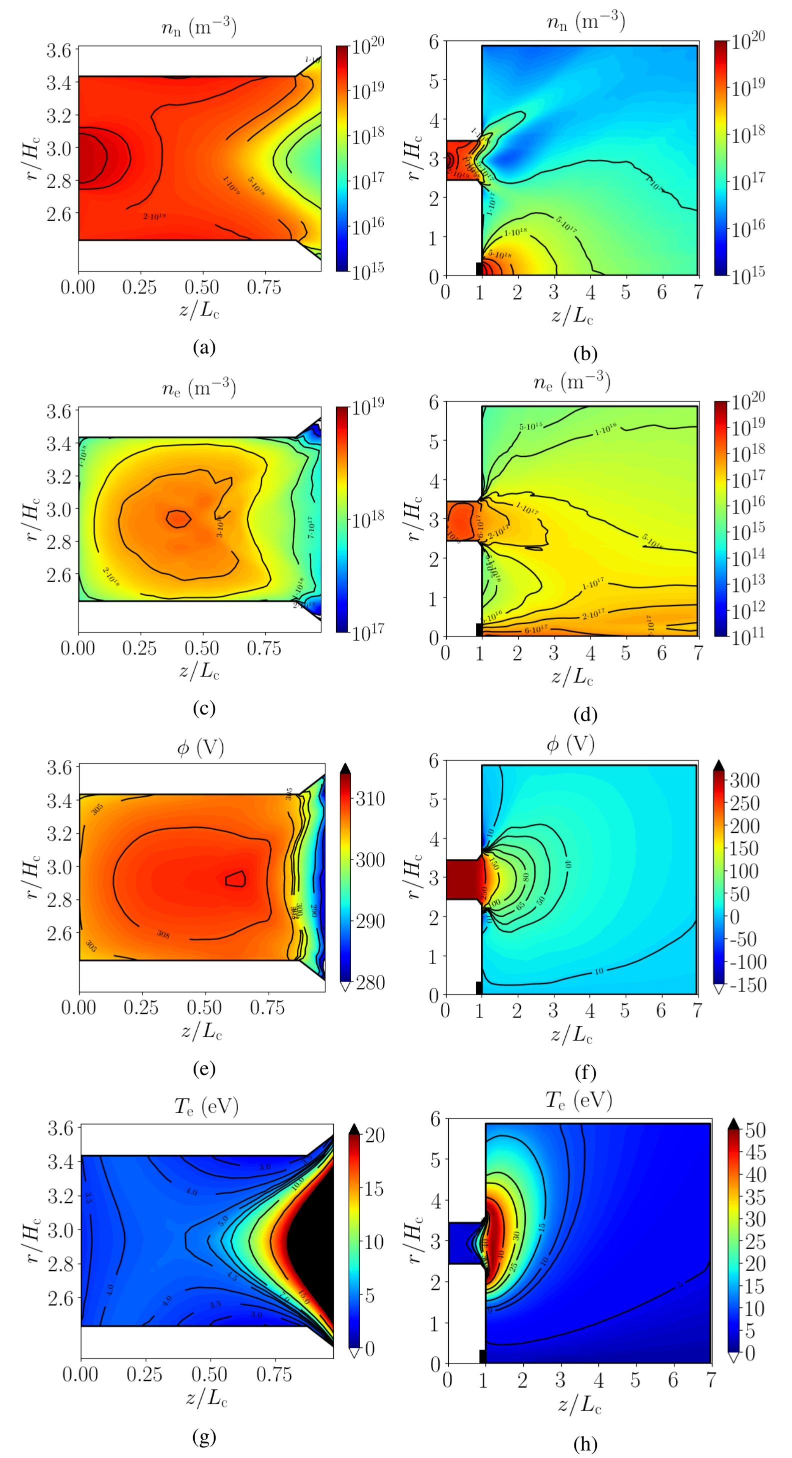

Fig. 6 Time-averaged 2D (z,r) contour maps for the reference case. (a)-(b) Neutral density n_n, (c)-(d) plasma density n_e, (e)-(f) electric potential ϕ and (g)-(h) electron temperature T_e. The left column plots show magnitudes inside the thruster chamber, while the right column plots correspond to the whole simulation domain. The centrally-mounted cathode is indicated by the small black box.

sheaths). Ion and electron current densities are identical at dielectric walls. At the anode, the backward ion current density is around a 20% of the electron current, which is still a percentage larger than desirable. This behaviour has

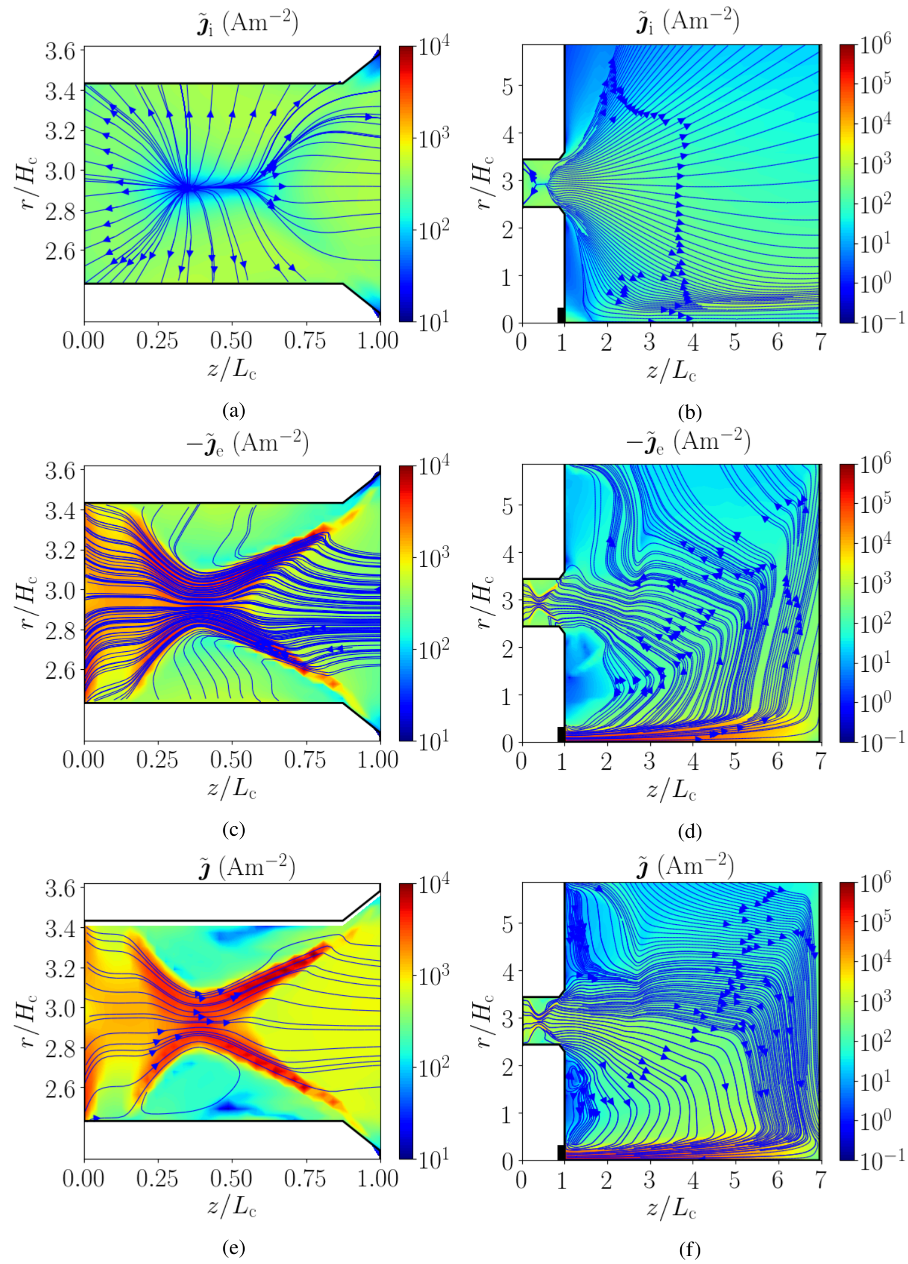

Fig. 7 Time-averaged 2D (z,r) contour maps for the reference case. Magnitude of the longitudinal (a)-(b) ion current density vector $\tilde{j}_{\mathrm{i}}$, (c)-(d) electron current density vector $\tilde{j}_{\mathrm{e}}$ and (e)-(f) electric current density vector $\tilde{j}$. Blue lines with arrows depict the streamlines of (a)-(b) $\tilde{j}_{\mathrm{i}}$, (c)-(d) $-\tilde{j}_{\mathrm{e}}$ and (e)-(f) $\tilde{j}$. The left column plots show magnitudes inside the thruster chamber, while the right column plots correspond to the whole simulation domain. The centrally-mounted cathode is indicated by the small black box close to the axis.

also been observed in the simulations of the HT5k thruster, featuring a similar magnetic topology [5]. Fig. 8(e) plots the average energy per ion particle impacting the wall $\mathcal{E}_{\mathrm{i,wall}}$. The low values of $\Delta\phi_{\mathrm{sh}}$ yield ion-impact energies below typical erosion thresholds [41, 42] along practically the whole chamber wall, which is the main advantage expected from magnetically shielded topologies. At the end of both chamfers, however, a significant increase of $\mathcal{E}_{\mathrm{i,wall}}$ is observed, reaching a maximum value of ~170 eV at chamber outer corner, which is mainly related to the ϕ drop close to the exit of the thruster chamber, already observed in Fig. 8(a), and also evident in Figs. 5(c), 6(e) and 6(f). This result suggests that a shorter thruster channel could help reducing this effect.

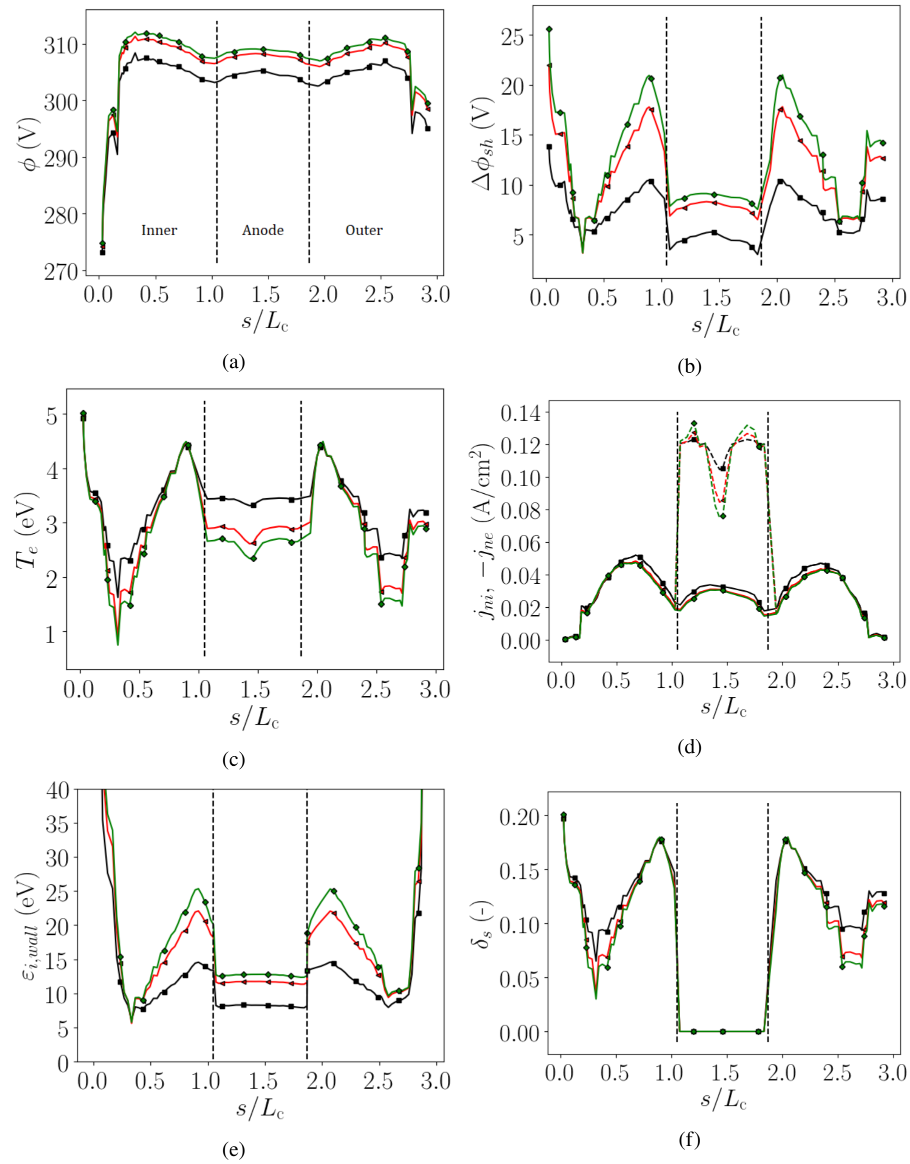

Fig. 8 Time-averaged 1D profiles along the thruster chamber walls for simulation cases with σ_{rp} = 0.1 (black line with square markers), σ_{rp} = 0.5 (red line with triangle markers) and σ_{rp} = 1.0 (green line with diamond markers). Coordinate s runs from the inner chamfer end to the outer chamfer end. Profiles of (a) electric potential at the sheath edge, ϕ; (b) potential fall across the sheath edge, $\Delta\phi_{\rm sh}$; (c) electron temperature at the sheath edge, $T_{\rm e}$; (d) ion (solid line), $j_{\rm ni}$, and electron (dashed line), $j_{\rm ne}$, current normal to the walls; (e) ion wall-impact energy, $\mathcal{E}_{\rm i,wall}$; and (f) SEE yield, $\delta_{\rm s}$.

B. Analysis of current and power balances and performances

The ion current balance at steady state can be expressed as

$$I_{\rm prod} = I_{\rm i\infty} + I_{\rm iD} + I_{\rm iA} + I_{\rm iC}, \tag{4}$$

with $I_{\rm prod}$ being the ion production rate in the whole simulation domain; $I_{\rm iD}$, $I_{\rm iA}$ and $I_{\rm iC}$, the ion currents impacting the dielectric, anode and cathode walls, respectively (and defined in Fig. 2(b)); and $I_{\rm i\infty}$, the ion beam current leaving the domain at plume (free loss) boundaries. This last term is the only one that contributes to the thrust. All currents are defined as positive; $I_{\rm prod}$ comes out from a volumetric integration, and the other ones are computed from surface integrals at the domain boundaries. Table. 4 contains the value of I_{prod} and how this is distributed among the different boundaries, considered in Eq. (4). I_{iC} is about one order of magnitude lower than I_{iA} and has not been included. The table also includes the propellant utilization, the current efficiency, and the charge efficiency, defined as

$$\eta_{\mathrm{u}} = \frac{\dot{m}_{\mathrm{i}\infty}}{\dot{m}}, \qquad \eta_{\mathrm{cur}} = \frac{I_{\mathrm{i}\infty}}{I_{\mathrm{d}}}, \qquad \eta_{\mathrm{ch}} = \frac{e\dot{m}_{\mathrm{i}\infty}}{m_{\mathrm{i}} I_{\mathrm{i}\infty}}, \tag{5}$$

respectively. Here $\dot{m} = \dot{m}_{\mathrm{A}} + \dot{m}_{\mathrm{C}}$, and $\dot{m}_{\mathrm{i}\infty}$ is the total ion mass flow across the plume boundaries. Compared to a typical discharge in a HET with a conventional magnetic topology, η_{u} and η_{cur} are rather good. The relative amount of doubly-charged ions in the discharge, measured by η_{ch}, is similar. The relative current losses to the lateral walls, $I_{\mathrm{iD}}/I_{\mathrm{prod}}$, are rather high compared to a conventional HET, and also higher than those found for the case of the HT5k [5]. The relative current losses to the anode, $I_{\mathrm{iA}}/I_{\mathrm{prod}}$, are closer to those of a conventional HET, and lower than in the HT5k case [5]. This value is likely affected by the position of the null point inside the chamber, which is not far away from the anode wall. Although further analyses are required, from the point of view of current losses to walls, the MS topology does not seem much advantageous with respect to a more conventional one. This conclusion is not applicable to the power losses analyses, as shown next.

Table 4 Value of I_{prod} and fractions of I_{prod} corresponding to the different contributions to the current balance in Eq. (4). Values of η_{u}, η_{cur} and η_{ch}, defined in Eq. (5).

Case	V_{s} (V)	$\dot{m}_{\mathrm{A}}$ (mg/s)	I_{prod} (A)	$I_{\mathrm{i}\infty}/I_{\mathrm{prod}}$	$I_{\mathrm{iD}}/I_{\mathrm{prod}}$	$I_{\mathrm{iA}}/I_{\mathrm{prod}}$	η_{u}	η_{cur}	η_{ch}
Ref	300	20	43.9	0.38	0.55	0.07	0.94	0.74	0.88

The plasma power balance for the steady state discharge is

$$P = P_{\infty} + P_{\mathrm{D}} + P_{\mathrm{A}} + P_{\mathrm{inel}}, \tag{6}$$

where $P = I_{\mathrm{d}} V_{\mathrm{d}} + P_{\mathrm{C}}$ is the total power deposited into the plasma discharge, sum of the discharge power and the net power delivered through cathode electron emission (P_{C} amounting to 1-2% of P); P_{∞} is the plasma energy flow through the plume boundaries; P_{D} and P_{A} are the power losses at the dielectric walls and anode, respectively; and P_{inel} corresponds to the power losses due to inelastic (ionization and excitation) collisions. All powers are defined as positive. P_{inel} is obtained from a volumetric integration over the whole simulation domain, P_{∞} comes from a surface integral at the plume boundaries, and P_{D} and P_{A} are computed from surface integrals at the respective walls (not at the Debye sheath edges). Eqs. (4) and (6) have also been used to check that the numerical errors of the HYPHEN simulations are acceptable (below 3% in all cases). Table. 5 lists contributions to the power balance in Eq. (6). Observe that whereas the current losses to the lateral walls amount to a 55% of I_{prod}, the energy losses to these walls are only a 7% of the input power. Adding the energy losses to the anode, the total energy losses to the chamber walls add up to just 10%, which can be considered a great achievement of the MS topology. Inelastic losses are consistent with the ion production: the ratio $P_{\mathrm{inel}}/I_{\mathrm{prod}}$ yields 23.2 eV as effective single-ionization cost (which includes the contribution from excitation collisions).

The thrust efficiency is defined and then factorized as

$$\eta = \frac{F^2}{2\dot{m}P} \equiv \eta_{\mathrm{ene}}\eta_{\mathrm{div}}\eta_{\mathrm{disp}}, \tag{7}$$

where F is the thrust, measured from plasma properties at the plume boundary. The relation between the thrust efficiency and the anodic efficiency is the following: $\eta = \eta_{\mathrm{A}}(\dot{m}_{\mathrm{A}}/\dot{m})$ The energy, divergence, and dispersion efficiencies are defined, respectively, as

$$\eta_{\mathrm{ene}} = \frac{P_{\infty}}{P} \qquad \eta_{\mathrm{div}} = \frac{P_{z\infty}}{P_{\infty}}, \qquad \eta_{\mathrm{disp}} = \frac{F^2}{2\dot{m}P_{z\infty}}, \tag{8}$$

with $P_{z\infty}$ being the flow of axial plasma energy across the plume free loss boundaries. With the definitions in Eq. (8), η_{ene} quantifies the fraction of input power in the downstream plume, η_{div} assesses the plume divergence using the axial energy and total energy flows in the plume, and η_{disp} quantifies the level of dispersion of velocity of all plasma species (which would be one for a mono-velocity gas). Plume energy flows include the residual energy of electrons, which is a consequence of their incomplete expansion in the finite simulation domain, but this is quite low: about 4%. Setting $\cos^2\alpha_{\mathrm{div}} = \eta_{\mathrm{div}}$, the half-divergence angles in these simulations are $\alpha_{\mathrm{div}} \sim 27$ deg. Here we find η = 51% or 54.7% for the "anodic" thrust efficiency, which is close to the experimentally reported value, 59.5%.

Table 5 Value of P and fractions of P corresponding to different contributions to the power balance in Eq. (6). Values of η, η_{ene}, η_{div} and η_{disp}, defined in Eq. (8).

Case	V_{s} (V)	$\dot{m}_{\mathrm{A}}$ (mg/s)	P (kW)	η	P_{inel}/P	P_{D}/P	P_{A}/P	P_{∞}/P (= η_{ene})	η_{div}	η_{disp}
Ref.	300	20	6.78	0.51	0.15	0.07	0.03	0.76	0.79	0.85

C. Plasma-wall interaction parameter sensitivity analyses

In this section, the sensitivity of the simulation results to some relevant plasma-wall parameters is carried out. In particular, Sec. V.C.1 reports the effects of the replenishment fraction of the electron VDF, σ_{rp}, while Sec. V.C.2 discusses the effects of the parameter E_{r} for the yield of elastically reflected electrons in Eq. (2).

1. Electron VDF replenishment fraction

The parameter σ_{rp} ranges from zero to one and models the partial depletion of the high energy tails of the electron VDF in the low-collisional plasma of a HET discharge. A small σ_{rp} value represents a large depletion of the high energy tails of the electron VDF, which affects particle and energy fluxes deposited to the thruster chamber walls.

Three different values σ_{rp} are considered here: 0.1 (reference case), 0.5 and 1. Changes in thruster performances are around 1-2% for all cases and no significant effects on the 2D maps of main plasma variables have been found. Fig. 8 shows the comparison of the plasma profiles along the thruster chamber walls. The black line with square markers correspond to the results for reference case (i.e., σ_{rp} = 0.1), already commented in Sec. V.A. The cases with σ_{rp} = 0.5 and 1 correspond to the red and green lines, with triangle and diamond markers, respectively. The main result is the increase in the sheath potential fall around the thruster chamber walls for larger σ_{rp} values, consistent with the corresponding larger replenishment of the high energy tails of the electron VDF. This fact yields higher ion-wall impact energies, although they are still well below erosion thresholds along most of the chamber walls. The slight decrease in the discharge current collected at the anode produces an increase of about 1% in the thrust efficiency. For all cases, the MS of the walls is effective in keeping a low electron temperature around the walls.

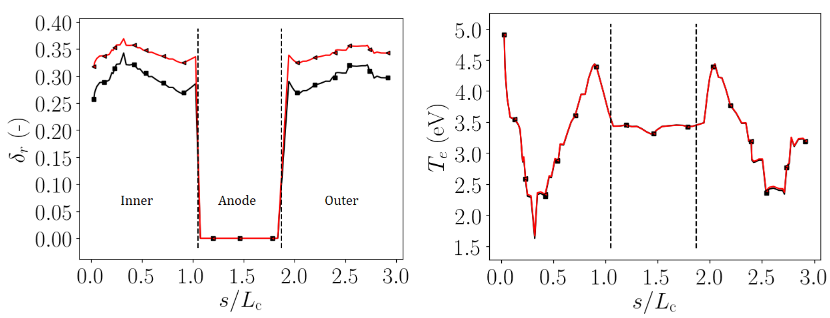

(a) (b)

Fig. 9 Time-averaged 1D profile along the thruster chamber walls for simulation cases with E_{r} = 20 eV (black line with square markers), E_{r} = 40 eV (red line with triangle markers). Coordinate s runs from the inner chamfer end to the outer chamfer end. Profiles of (a) reflected electrons yield δ_{r} and (b) electron temperature T_{e}.

2. Elastically reflected electrons

The parameter E_{r} affects the yield of elastically reflected electrons at dielectric walls according to Eq. (2). At a given T_{e}, the higher E_{r} the higher δ_{r}. Two simulation cases featuring E_{r} = 20 eV (reference case) and 40 eV are compared in this section.

In Fig. 9(a), the yield of reflected electrons is observed to increase at the dielectric walls with the increment in E_{r}, since the electron temperature remains roughly unchanged, as seen in Fig. 9(b). The impact of this variation of δ_{r} is not significant in the thruster performance nor in the relevant plasma properties.

D. Plume effects

1. Effects of cathode injection mass flow

In this section, the effect of neutral gas injection through the centrally-mounted cathode is studied. The results for the reference simulation case with and without neutral gas injection through the cathode are compared.

Fig. 5 shows the time-averaged 1D profiles of the relevant plasma magnitudes along the thruster channel midline. Cases with and without neutral gas injection through the cathode correspond to black lines with square markers and red lines with circle markers, respectively. The plasma density along the thruster channel midline is barely affected by the neutral injection through the cathode. On the other hand, the increase of n_n along the near plume when injection is active, due to the presence of the cathode neutral plume, is absent when the neutral injection is deactivated, and the neutral density profiles remains nearly flat and about one order of magnitude lower. A similar trend is found for the neutral pressure in the near plume. The reduced electron Joule heating in the vicinity of the thruster chamber exit yields a lower electron temperature peak there. Moreover, the lower electron-neutral collisionality yields and a weaker coupling between the cathode electrons and the ion beam, thus resulting in a larger coupling voltage in the near plume, and a 4% decrease in thrust with respect to the case with neutral injection. A 2% decrease in I_d is also found.

2. Effects of charge-exchange collisions

The effects of charge-exchange (CEX) collisions in the simulation results of the reference case are analyzed in this section.

Fig. 10(a) compares the results of the reference simulation case with and without CEX collisions. The 1D axial profiles of ϕ reveals a negligible effect of CEX collisions in the time-averaged plasma discharge. As shown in Fig. 10(b), inside the thruster chamber, the densities of both singly and doubly-charged CEX ions (i.e. ions resulting from a CEX collision) can reach local values of about 20-30% of the corresponding singly and doubly charged ion populations resulting from ionization collisions.

Fig. 10(c) shows the time-averaged 2D map of the CEX-to-ionization density ratio for singly charged ions. Focusing on the near plume region, for $r > r_c$ the CEX ions density is below 15-20% of the ionization ions density, reaching its peak in the external lateral part of the plume, as expected. However, both ion densities are of the same order in the core of the plume, along the symmetry axis. This effect is mainly due to CEX collisions in the cathode plume, enhanced by the neutral injection through the cathode. The expansion of fast CEX neutrals generated in this region yields a lower neutral density there, as shown in Fig. 10(d).

E. Far plume boundary condition and stray currents

In this section, the effects of the boundary condition imposed at the plume downstream boundary P, identified by the thick blue line at the downstream end of the simulation domain in Fig. 3, are explored. The GDML model summarized in Sec. III is applied at the boundary P. The different cases compared here are listed in Table. 6. The first row contains the results of the reference case, for which the final potential at infinity reaches the value $\phi_{\infty,0}$ = -5.3 V (with respect to cathode), for which the net current collected at the downstream plume boundary is zero at any time instant (i.e. $I_\infty = 0$). The second and third rows of Table. 6 correspond to simulation cases for a fixed final potential value equal to $\phi_\infty = 1.2\phi_{\infty,0}$ and $\phi_\infty = 0.8\phi_{\infty,0}$, respectively, so that a certain current I_∞ is collected at the plume downstream boundary, as sketched in Fig. 3.

This simulation scenario with HYPHEN code is not intended to reproduce the effects of the actual stray currents measured during real thruster operation in direct drive configuration. This study is being performed with EP2PLUS code, and is to be reported in the deliverable D6.3. Therefore, the main aim here is to assess the performance of the new GDML model developed for the challenging downstream boundary conditions in the near plume of a HET discharge, and to evaluate the effect of the infinity-to-cathode bias ϕ_∞ on the discharge.

The main result of this analysis is that the time-average value of I_d is minimally affected ($\Delta I_d \sim 1\%$) when $\Delta\phi_\infty$ = 20% of $\phi_{\infty,0}$. For these cases, a current I_∞ ~5-6% of I_d flows between the downstream boundary and the cathode. Here, the electron and ion contributions to I_∞ are considered positive and negative, respectively. This result indicates that the anode-to-cathode plasma bridge is barely affected by ϕ_∞ variation. The time-average plasma maps in the bulk domain does not exhibit significant variations and have been omitted.

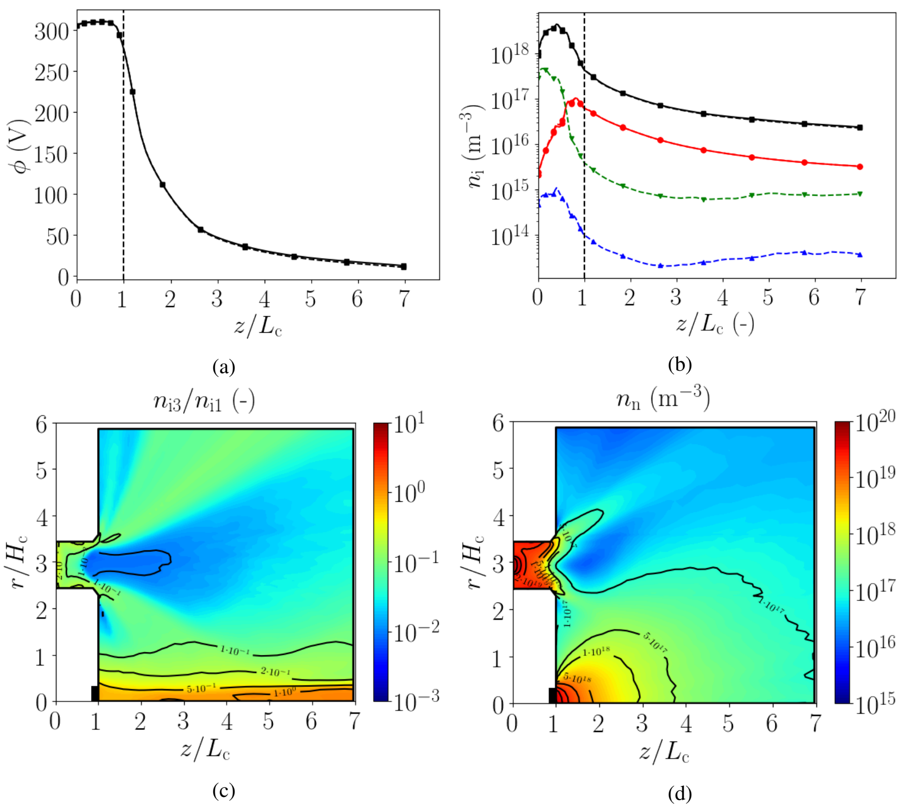

Fig. 10 Time-averaged 1D axial profiles along the thruster channel midline for cases without CEX (solid line) and with CEX (dashed line). (a) Density of singly-charged ions, n_{i1}, (black line with square markers), doubly-charged ions, n_{i2}, (red line with circle markers), singly-charged CEX ions, n_{i3}, (green line with down triangle markers), doubly-charged CEX ions, n_{i4}, (blue line with up triangle markers), (b) electric potential ϕ, (c) ratio of n_{i3}/n_{i1} and (d) neutral density n_n for the case with CEX collisions.

Table 6 Results for the simulation cases with different infinity-to-cathode potential bias.

Case	ϕ_∞ (V)	I_∞ (A)	I_∞/I_d (%)	$I_d(A)$
$\phi_\infty = \phi_{\infty,0}$	-5.3	0.0	0.0	22.6
$\phi_\infty = 1.2\phi_{\infty,0}$	-6.3	-1.38	-6.1	22.8
$\phi_\infty = 0.8\phi_{\infty,0}$	-4.3	1.17	5.2	22.6

VI. Conclusions

HYPHEN numerical simulations of SITAEL's HT20k prototype with MS topology and a central cathode for a single operation point with xenon as propellant have been presented in this work.

Electron turbulence transport has been modeled through a two parameter $(\alpha_{t1}, \alpha_{t2})$ step-out profile for a phenomenological anomalous collision frequency, which has been fitted to match the experimental data (I_d, F), provided by SITAEL, with errors below 5%. The fitting has been proven to capture the thruster breathing mode, thus partially validating the simulation results. A fully 2D description of the plasma discharge has been detailed for a single operation point, with special focus on effects related to MS topology, the central cathode and the plasma plume expansion in free space. The MS topology moves most of the acceleration region outside the thruster chamber, and yields a high-density and low-temperature plasma inside the thruster chamber. MS effects include low (1) electron temperature around the thruster chamber walls, (2) ion wall-impact energy (below typical erosion thresholds in most of the chamber walls) and (3) plasma losses to the walls. Sensitivity analyses on relevant plasma-wall related parameters have shown limited influence on the plasma discharge and thruster performance.

In the near plume, a central cathode with both electron and neutral emission has been simulated. Cathode electrons split into a downstream neutralizing beam, and a upstream beam that drifts towards the interior of the thruster chamber. The latter is channeled by the magnetic lines close to the magnetic null point inside the thruster chamber, and a small fraction is collected to the lateral walls to cancel the ion flow and satisfy the dielectric wall condition. The injection of neutrals through the cathode has been shown to improve the cathode-beam coupling in the near plume, thus yielding a higher thrust. On the other hand, CEX collisions, also enhanced by the neutral injection through the cathode, are shown to slightly affect the plasma discharge maps and thruster performances.

A new GDML model has permitted to address the effect of electric currents collected at the plume downstream boundary by acting on the infinity-to-cathode bias ϕ_∞. The main result is that I_d is barely affected (~1% variation) for collected currents I_∞ ~5-6% of I_d, the latter flowing between cathode and infinity.

Future work includes the simulation of different HT20k operation points in DD architecture, and a deeper analysis of relevant aspects, including the plasma interaction with the MS thruster walls, the plume expansion and the cathode-beam coupling processes.

Aknowledgements

This work has been supported by the ASPIRE project, funded by the European Union's Horizon 2020 Research and Innovation Programme, under Grant Agreement 101004366.

References

[1] Andreussi, T., Piragino, A., Reza, M., Gianetti, V., Faraji, F., Ferrato, E., Pedrini, D., Kitaeva, A., Rossodivita, A., and Andrenucci, M., "Development status and way forward of SITAEL's 20kW class Hall thruster, the HT20k," 36^{th} *International Electric Propulsion Conference, Vienna, Austria*, 2019.

[2] Piragino, A., Ferrato, E., Faraji, F., Reza, M., Giannetti, V., Kitaeva, A., Pedrini, D., Andrenucci, M., and Andreussi, T., "SITAEL's magnetically shielded 20 kW Hall thruster tests," 36^{th} *International Space Propulsion Conference 2019, Vienna, Austria*, 2019.

[3] Domínguez-Vázquez, A., "Axisymmetric simulation codes for Hall effect thrusters and plasma plumes," Ph.D. thesis, Universidad Carlos III de Madrid, Leganés, Spain, 2019.

[4] Domínguez-Vázquez, A., Zhou, J., Fajardo, P., and Ahedo, E., "Analysis of the plasma discharge in a Hall thruster via a hybrid 2D code," 36^{th} *International Electric Propulsion Conference*, Electric Rocket Propulsion Society, Vienna, Austria, 2019.

[5] Perales-Díaz, J., Domínguez-Vázquez, A., Fajardo, P., Ahedo, E., Faraji, F., Reza, M., and Andreussi, T., "Hybrid plasma simulations of a magnetically shielded Hall thruster," *Journal of Applied Physics*, Vol. 131, No. 10, 2022. https://doi.org/10.1063/5.0065220.

[6] Domínguez-Vázquez, A., Zhou, J., Sevillano-González, A., Fajardo, P., and Ahedo, E., "Analysis of the electron downstream boundary conditions in a 2D hybrid code for Hall thrusters," 37^{th} *International Electric Propulsion Conference*, Electric Rocket Propulsion Society, Boston, MA, June 19-23, 2022.

[7] Piragino, A., Leporini, A., Giannetti, V., Pedrini, D., Rossodivita, A., Andreussi, T., and Andrenucci, M., "Characterization of a 20 kW class Hall effect thruster," 35^{th} *International Electric Propulsion Conference 2019*, 2017.

[8] Andreussi, T., Giannetti, V., Leporini, A., Saravia, M. M., and Andrenucci, M., "Influence of the magnetic field configuration on the plasma flow in Hall thrusters," *Plasma Phys. Control. Fusion*, Vol. 60, No. 1, 2018.

[9] Gianetti, V., Ferrato, E., Piragino, A., Reza, M., Faraji, F., Andrenucci, M., and Andreussi, T., "HT5k Thruster Unit Development History, Status and Way Forward," *Proc. 36th International Electric Propulsion Conference, Vienna, Austria*, 2019.

[10] Mikellides, I., Katz, I., Hofer, R., Goebel, D., de Grys, K., and Mathers, A., "Magnetic shielding of the channel walls in a Hall plasma accelerator," *Physics of Plasmas*, Vol. 18, 2011, p. 033501.

[11] Piragino, A., Faraji, F., Reza, M., Ferrato, E., Piraino, A., and Andreussi, T., "Background Pressure Effects on the Performance of a 20 kW Magnetically Shielded Hall Thruster Operating in Various Configurations," *Aerospace*, Vol. 8, No. 3, 2021, p. 69.

[12] Pedrini, D., Misuri, T., Paganucci, F., and Andrenucci, M., "Development of Hollow cathodes for space electric propulsion at Sitael," *Aerospace*, Vol. 4, 2017. https://doi.org/https://doi.org/10.3390/aerospace4020026.

[13] Giannetti, V., Piragino, A., Paissoni, C., Ferrato, E., Estublier, D., and Andreussi, T., "Numerical and Experimental Investigation of Longitudinal Oscillations in Hall Thrusters," *Journal of Applied Physics*, Vol. 131, 2022, p. 013304. https://doi.org/https://doi.org/10.1063/5.0070945.

[14] Andreussi, T., Piragino, A., Giannetti, V., Kitaeva, A., Paissoni, C., Ferrato, E., Pedrini, D., Rossodivita, A., Broggi, N., P. Hildebrand, and Dartsch, H., "Development tests of SITAEL's high power propulsion systems," *Space Propulsion Conference*, 2022.

[15] Domínguez-Vázquez, A., Cichocki, F., Merino, M., Fajardo, P., and Ahedo, E., "Axisymmetric plasma plume characterization with 2D and 3D particle codes," *Plasma Sources Science and Technology*, Vol. 27, No. 10, 2018, p. 104009. https://doi.org/10.1088/1361-6595/aae702.

[16] Domínguez-Vázquez, A., Cichocki, F., Merino, M., Fajardo, P., and Ahedo, E., "On heavy particle-wall interaction in axisymmetric plasma discharges," *Plasma Sources Science and Technology*, Vol. 30, No. 8, 2021, p. 085004. https://doi.org/10.1088/1361-6595/ac1715, URL https://doi.org/10.1088/1361-6595/ac1715.

[17] Pérez-Grande, D., González-Martínez, O., Fajardo, P., and Ahedo, E., "Analysis of the numerical diffusion in anisotropic mediums: benchmarks for magnetic field aligned meshes in space propulsion simulations," *Applied Sciences*, Vol. 6, No. 11, 2016, p. 354.

[18] Zhou, A., J. Domínguez-Vazquez, Fajardo, P., and Ahedo, E., "Magnetized fluid electron model within a two-dimensional hybrid simulation code for electrodeless plasma thrusters," *Plasma Sources Science and Technology*, accepted for publication.

[19] Fife, J. M., "Hybrid-PIC modeling and electrostatic probe survey of Hall thrusters," Ph.D. thesis, Massachusetts Institute of Technology, 1998.

[20] Boeuf, J., and Garrigues, L., "Low frequency oscillations in a stationary plasma thruster," *J. Applied Physics*, Vol. 84, No. 7, 1998, pp. 3541–3554.

[21] Ahedo, E., Gallardo, J., and Martínez-Sánchez, M., "Effects of the radial-plasma wall interaction on the axial Hall thruster discharge," *Physics of Plasmas*, Vol. 10, No. 8, 2003, pp. 3397–3409.

[22] Parra, F., Ahedo, E., Fife, M., and Martínez-Sánchez, M., "A two-dimensional hybrid model of the Hall thruster discharge," *Journal of Applied Physics*, Vol. 100, 2006, p. 023304.

[23] Zhou, J., Pérez-Grande, D., Fajardo, P., and Ahedo, E., "Numerical treatment of a magnetized electron fluid within an electromagnetic plasma thruster code," *Plasma Sources Science and Technology*, Vol. 28, No. 11, 2019, p. 115004.

[24] Zhou, J., "Modeling and simulation of the plasma discharge in a radiofrequency thruster," Ph.D. thesis, Universidad Carlos III de Madrid, Leganés, Spain, 2021.

[25] Pérez-Grande, D., "Fluid modeling and simulation of the electron population in Hall effect thrusters with complex magnetic topologies," Ph.D. thesis, Universidad Carlos III de Madrid, Leganés, Spain, 2018.

[26] Mikellides, I., Katz, I., Goebel, D. M., Jameson, K. K., and Polk, J. E., "Wear mechanisms in electron sources for ion propulsion, 2: Discharge hollow cathode," *Journal of Propulsion and Power*, Vol. 24, No. 4, 2008, pp. 866–879.

[27] Stephen Francis Biagi, "Cross sections extracted from PROGRAM MAGBOLTZ, VERSION 7.1 JUNE 2004," , June 2004. URL www.lxcat.net/Biagi-v7.1, [Online; accessed 5-July-2021].

[28] Mitchner, M., and Kruger Jr., C., *Partially ionized gases*, John Wiley and Sons, Hoboken, NJ, 1973.

[29] Mazouffre, S., Echegut, P., and Dudeck, M., "A calibrated infrared imaging study on the steady state thermal behaviour of Hall effect thrusters," *Plasma Sources Science and Technology*, Vol. 16, No. 1, 2006, p. 13.

[30] Moore, P., and Sowter, A., "Application of a satellite aerodynamics model based on normal and tangential momentum accommodation coefficients," *Planetary and space science*, Vol. 39, No. 10, 1991, pp. 1405–1419.

[31] Moe, K., and Moe, M., "Gas–surface interactions and satellite drag coefficients," *Planetary and Space Science*, Vol. 53, No. 8, 2005, pp. 793–801.

[32] Ahedo, E., and Pablo, V. d., "Combined effects of electron partial thermalization and secondary emission in Hall thruster discharges," *Physics of Plasmas*, Vol. 14, 2007, p. 083501.

[33] Araki, S., and Wirz, R., "Magnetic Field Aligned Mesh for Ring-Cusp Discharge Chambers," *50th AIAA/ASME/SAE/ASEE Joint Propulsion Conference & Exhibit*, Cleveland, Ohio, US, 2014.

[34] Hagelaar, G., Bareilles, J., Garrigues, L., and Boeuf, J., "Role of anomalous electron transport in a stationary plasma thruster simulation," *Journal of Applied Physics*, Vol. 93, No. 1, 2003, pp. 67–75.

[35] Koo, J., and Boyd, I., "Modeling of anomalous electron mobility in Hall thrusters," *Physics of Plasmas*, Vol. 13, 2006, p. 033501.

[36] Santos, R., "Código híbrido avanzado de motores de plasma de efecto Hall," Ph.D. thesis, Universidad Politécnica de Madrid (UPM), Madrid, Spain, 2012.

[37] Bareilles, J., Hagelaar, G., Garrigues, L., Boniface, C., Boeuf, J., and Gascon, N., "Critical assessment of a two-dimensional hybrid Hall thruster model: Comparisons with experiments," *Physics of Plasmas*, Vol. 11, No. 6, 2004, pp. 3035–3046.

[38] Fife, J., Martínez-Sánchez, M., and Szabo, J., "A Numerical Study of Low-Frequency Discharge Oscillations in Hall Thrusters," *33rd Joint Propulsion Conference, Seattle, WA*, 1997.

[39] Choueiri, E., "Plasma oscillations in Hall thrusters," *Physics of Plasmas*, Vol. 8, No. 4, 2001, pp. 1411–1426.

[40] Barral, S., and Ahedo, E., "Low-frequency model of breathing oscillations in Hall discharges," *Physical Review E*, Vol. 79, 2009, p. 046401.

[41] Mikellides, I. G., Hofer, R. R., Katz, I., and Goebel, D. M., "Magnetic shielding of Hall thrusters at high discharge voltages," *Journal of Applied Physics*, Vol. 116, 2014, p. 053302.

[42] Brown, N. P., and Walker, M. L. R., "Review of plasma-induced hall thruster erosion review of plasma-induced hall thruster erosion," *Applied Sciences*, Vol. 10, No. 11, 2020, p. 3775.